

# Non-invasive laser Doppler perfusion measurements of large tissue volumes and human skeletal muscle blood RMS velocity

T Binzoni<sup>1</sup>, T S Leung<sup>2</sup>, D Boggett<sup>3</sup> and D Delpy<sup>2</sup>

<sup>1</sup> Departments of Radiology and Physiology, Faculty of Medicine, University of Geneva, Switzerland

<sup>2</sup> Department of Medical Physics and Bioengineering, University College London, UK

<sup>3</sup> Moor Instruments Ltd, Millwey Axminster, Devon, UK

E-mail: Tiziano.Binzoni@medecine.unige.ch

Received 30 January 2003

Published 22 July 2003

Online at [stacks.iop.org/PMB/48/2527](http://stacks.iop.org/PMB/48/2527)

## Abstract

This study proposes the implementation of an algorithm allowing one to derive absolute blood root-mean-square (RMS) velocity values from laser Doppler perfusion meter (LDP) data. The algorithm is based on the quasi-elastic light scattering theory and holds for multiple scattering. While standard LDP measurements are normally applicable to a small region of interest ( $\sim 1 \text{ mm}^2$ ), the present method allows the analysis of both small and large tissue volumes with small and large interoptode spacings (e.g., 1.5 cm). The applicability and the limits of the method are demonstrated with measurements on human skeletal muscle using a custom-built near-infrared LDP meter. Human *brachioradialis* muscle RMS velocity values of  $9.99 \pm 0.01$  and  $5.58 \pm 0.03 \text{ mm s}^{-1}$  at 1.5 cm and of  $5.18 \pm 0.01$  and  $2.54 \pm 0.09 \text{ mm s}^{-1}$  at 2 cm were found when the arm was (a) at rest and (b) occluded, respectively. At very large optode spacings or very high moving particle densities, the theory developed here would need to be amended to take into account second-order effects.

## 1. Introduction

Monitoring the metabolic activity of human tissues (e.g., skeletal muscle, brain, etc) is of fundamental importance for patho-physiological studies or clinical diagnosis. Near-infrared spectroscopy (NIRS) (Chance *et al* 1997) and magnetic resonance imaging (MRI) (McCully *et al* 1999) are two non-invasive techniques allowing such information to be obtained. Both methods are based on the fact that they are sensitive to the  $\text{O}_2$  saturation changes of haemoglobin. Changes in metabolic activity are usually estimated by directly measuring oxy- and deoxyhaemoglobin with NIRS (Delpy and Cope 1997) or, indirectly, by utilizing the

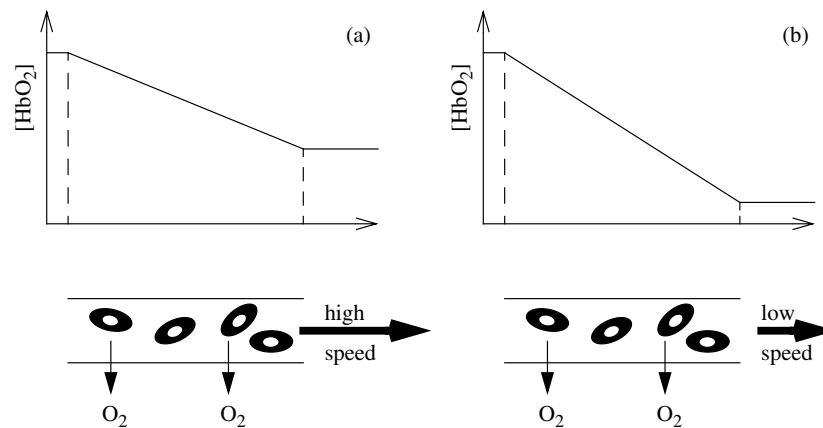


**Figure 1.** Oxyhaemoglobin concentration ( $[\text{HbO}_2]$ ) along a capillary. The capillary is represented by a tube containing erythrocytes (black bodies). In (a) the blood RMS velocity is higher than in (b). The oxygen consumption of the tissue is assumed to be the same in (a) and in (b). The lower perfusion condition will result in a lower blood oxygen content at the capillary output, in (b) (i.e., higher oxygen extraction) than in (a).

'BOLD effect' in MRI (Ugurbil *et al* 1999) induced by the presence of deoxyhaemoglobin. Unfortunately, tissue haemoglobin saturation depends not only on metabolic activity but also on blood velocity (see figure 1 for an intuitive representation), and the relationship existing between tissue metabolism and blood velocity is not simple (Cerretelli and Binzoni 1997). As a consequence, it is very difficult to distinguish real metabolic changes from variations of the NIRS or MRI signals induced by simple blood perfusion changes. This technical problem can lead to the incorrect physiological or clinical interpretation of data. For this reason, a new type of near-infrared laser Doppler based perfusion meter (LDP), allowing the measurement of a tissue perfusion index deep within the tissues (e.g., under the skin or skull surface) has previously been developed (Soelkner *et al* 1997, Lohwasser and Soelkner 1999, Binzoni *et al* 2002). The LDP is compatible with NIRS and MRI and thus should allow one to better understand the physiological data obtained with these techniques. Strictly speaking, the term 'blood flow speed' should be used instead of 'blood flow velocity' because this quantity is not directional. The term blood velocity is however used here for consistency with the literature on the topic.

The blood root-mean-square (RMS) velocity derived from conventional LDP instruments with small optode spacing is based on a series of classical algorithms (Obeid 1993) specifically designed for the estimation of blood perfusion in the skin (sampled volume: a fraction of  $\text{mm}^3$ ). Although these algorithms have been developed in a generalized form, only an approximation of the original formulation is usually used. The simplified form of the algorithms is however not entirely appropriate for the investigation of large tissue volumes (sampled volume: more than a  $\text{cm}^3$ ). Moreover, when it is necessary to compare different subjects, the classical approach imposes a calibration procedure that it is often not possible to realize *in vivo* (Leahy *et al* 1999).

Thus, based on previous studies and a well-tested mathematical approach (Bonner *et al* 1981, Bonner and Nossal 1981), the aim of this paper is to implement a new algorithm, which can be applied to both small and large tissue volumes, to compute blood RMS velocity in absolute values. Some experimental and theoretical results are presented and the limitations of this approach discussed in the light of the data.

## 2. Methods

The derivation of the present algorithm is based on a mathematical description of the behaviour of the light interacting with a biological tissue containing moving particles, e.g., erythrocytes in the blood (Bonner *et al* 1981) or with other moving bodies, e.g., a Petri dish containing bacteria (Nossal *et al* 1971). The equation obtained represents the power spectrum of the detected photoelectric current (i.e., the current produced by the laser light on a photodetector, after interaction with the tissue). The idea is to 'fit' the model to the experimental photoelectric current power spectrum data obtained with the LDP and hence deduce the RMS velocity of the moving bodies (in our case the erythrocytes). The RMS velocity will appear as one of the fitting parameters.

### 2.1. The laser Doppler instrument

The experimental data were obtained from a new LDP instrument already presented elsewhere (Binzoni *et al* 2002). Briefly, a commercially available LDP monitor, made by Moor Instruments Ltd (Millwey Axminster, Devon, UK), has been modified by the inclusion, in addition to the normal pin photodiode detector, of a second detector channel employing a Hamamatsu C5460-01 avalanche photodiode (APD) detector. The frequency response is dc to 100 kHz (response flat to 70 kHz). In addition, the normal laser source (typically 1–2 mW output) has been replaced with a 780 nm laser delivering approximately 33 mW from the optical probe. The laser light is delivered via a 210 cm long 400/430  $\mu\text{m}$  (core/hard cladding diameters) fibre and collected by a bundle of  $4 \times 400/430 \mu\text{m}$  fibres (core/hard cladding diameters; length 120 cm). The numerical aperture of the optical fibres (HCS, Spectran, USA) was 0.22. Both fibres are terminated at one end by an optical straight tip connector and at the other end by a 6 mm diameter black acetal cylinder. The detected photocurrent signal from the LDP monitor is low pass filtered by an antialiasing filter with a cut-off frequency of 25 kHz. The ac and the dc components of the signal are sent to the two bayonet nut connector outputs of the LDP (in the text ac and dc, respectively). The ac and dc signals are then sampled at 65 kHz by a PC-based analogue-to-digital conversion card (PCI-DAS1602/16, ComputerBoards Inc., Middleboro, MA, USA). Software has been written in Matlab 6 language (The MathWorks Inc., Natick, MA, USA) to acquire, process and display the LDP data in real-time.

This software acquires 2048 ac data points per acquisition, applies a Hanning window, calculates the power spectrum and averages over a preset number of power spectra before storing the results on the disk. In the same manner dc data points are acquired, but only the mean value is stored (one mean dc value for one stored power spectrum). The overall sampling frequency is 2 Hz.

The LDP is able to perform measurements at large spacing (e.g., up to 2 cm) between the ends of the two fibre optics connected to the laser source and the detector, respectively. This allows the light to reach deep regions of the tissue and resulting in a larger sampling volume. For example, at 2 cm spacing, the light penetration into tissue is estimated to be approximately 0.8–1.4 cm deep.

### 2.2. The mathematical model

The ac power spectra and dc values obtained from the LDP and stored on the PC hard disk were processed offline to obtain the blood RMS velocity ( $\text{mm s}^{-1}$ ). In this section we will describe how to derive analytically the power spectrum,  $P_{\text{APD}}(\omega)$ , where  $\omega = 2\pi\nu$  is the angular frequency and  $\nu$  the frequency in Hz of the ac component of the photocurrent. It must

be noted that  $P_{\text{APD}}(\omega)$  will describe the power spectrum of the photoelectric current at the APD level expressed in units of ampere, while the equivalent ac power spectrum obtained at the output of the LDP ( $P_{\text{LDP}}(\omega)$ ) is expressed in volts. The relationship existing between the two power spectra is thus the following:

$$P_{\text{LDP}}(\omega) = B^2 \times C^2 \times A^2 \times P_{\text{APD}}(\omega) \quad (1)$$

where  $B$  is the APD gain,  $C$  is the current to voltage conversion and  $A$  is the voltage gain utilized to amplify the small ac signal. The dc current at the APD level ( $i_0$ ) is related to the dc at the LDP output in the same manner as

$$\text{dc} = B \times C \times i_0. \quad (2)$$

In this case the term  $A$  is not present because it was not necessary to amplify the large dc signal. For the sake of clarity, we will introduce the model sample  $\hat{P}_{\text{APD}}(\omega_n)$ , describing  $P_{\text{APD}}(\omega_n)$ , without the use of the Hanning window. Later in the text, we will explain how it is also possible to take into account the Hanning window in the model, although this actually has a negligible effect on the computed parameters. For this reason, all the results will be given without the introduction of the windowing procedure. For simplicity, from now on all the indices  $n$  appearing in the equations will be neglected if not necessary for the explanation.

In general the relationship existing between the  $P_{\text{APD}}(\omega)$  and the fluctuating light intensity coming out from the tissue (Cummins and Swinney 1970, Bonner *et al* 1981) is given as

$$P_{\text{APD}}(\omega) = i_0^2 \delta(\omega) + \frac{qi_0}{\pi} + D(\omega) + i_0^2 S(\omega) \quad (3)$$

where  $q \cong -1.602 \times 10^{-19}$  C is the charge on the electron,  $\delta(\omega)$  is as usual the Dirac function (s), and  $S(\omega)$  the power spectrum of the ac component without the  $i_0^2$  term. The term  $i_0^2 \delta(\omega)$ , on the right-hand side of equation (3), is generated by the dc component of the signal (before the power spectrum calculation). The term  $\frac{qi_0}{\pi}$  is the shot noise and is negligible in the present case. The amplifier noise is represented by  $D(\omega)$ .

The first three terms on the right-hand side of equation (3) will act as constant baseline offsets and can be neglected in establishing the model. The focus here is on deriving an analytical form for  $i_0^2 S(\omega)$  valid for the physical/biological system one wants to describe. The function  $S(\omega)$  in principle contains the information allowing the computation of the blood RMS velocity. The theoretical derivation of  $S(\omega)$  is a well-known procedure (see, for an introduction, Johnson and Gabriel (1981)), and we only summarize the main steps below. The hypotheses and mathematical procedures necessary to derive  $S(\omega)$  may be found, for example, in Bonner *et al* (1981), Bonner and Nossal (1981) and Johnson and Gabriel (1981), although some minor errors in the original papers are corrected here (e.g., in Bonner and Nossal (1981), the term  $(i_o - i_{sc})^2$  was not printed in equation (4); the factor  $\frac{1}{2}$  was forgotten in equation (14)). Some explanations are also given in the appendix.

The present model is based on the quasi-elastic scattering theory and holds for multiple scattering. The derivation will follow the Bonner and Nossal procedure but, to be of general validity, it will not use the approximations leading to the assumptions of small tissue volumes (small optode spacing). For this reason, the normalized temporal autocorrelation function ( $g^{(2)}(\tau)$ ) utilized to describe the physical system is expressed in its complete form as (Bonner and Nossal 1981, Boas 1996):

$$g^{(2)}(\tau) = 1 + \beta \frac{(i_o - i_{sc})^2 + 2(i_o - i_{sc})i_{sc}|I(\tau)| + i_{sc}^2|I(\tau)|^2}{i_0^2} \quad (4)$$

where  $0 < \beta < 1$  is an instrumental factor which depends upon the optical coherence of the signal at the detector surface (Cummins and Swinney 1970),  $I(\tau)$  is the intermediate

scattering function of the Doppler-shifted light. The dc current intensity produced by the total light falling upon the photodetector is designated as  $i_o$  and the intensity of that portion which arises from photons that have interacted with moving cells is designated as  $i_{sc}$ .

Following the same procedure as in Bonner and Nossal (1981) it is possible to demonstrate that

$$I(\tau) = \frac{e^{\bar{m}(I_1(\tau)-1)} - e^{-\bar{m}}}{1 - e^{-\bar{m}}} \tag{5}$$

where  $I_1(\tau)$  is the normalized autocorrelation function for photons that experience only one collision with a moving particle before emerging from the tissue and  $\bar{m}$  is the average number of collisions which a detected photon makes with a moving cell. The parameter  $\bar{m}$  may also be interpreted in the following manner: the probability that a photon makes  $m$  collisions with a moving erythrocyte before emerging from the tissue may be described by a Poisson distribution where  $\bar{m}$  appears as the ‘lambda factor’ of the distribution:

$$P_m \equiv \frac{\bar{m}^m e^{-\bar{m}}}{m!}. \tag{6}$$

In the case of biological tissues with a uniformly distributed capillary bed (muscle, brain, etc),  $I_1(t)$  may be expressed in a simple way:

$$I_1(t) = \frac{1}{1 + \left(\frac{\langle V^2 \rangle^{\frac{1}{2}} t}{\sqrt{12\xi} a}\right)^2} \tag{7}$$

where  $a$  is the radius of an average spherical scatterer ( $2.75 \mu\text{m}$  for red blood cells), and  $\xi$  is a constant (0.1 for red blood cells) related to the shape of the moving particles.

$S(\omega)$  is expressed as

$$S(\omega) = \frac{1}{\pi} \int_{-\infty}^{+\infty} e^{i\omega\tau} [g^{(2)}(\tau) - 1] d\tau. \tag{8}$$

By combining equations (4)–(8) one finds the general expression for  $S(\omega)$ :

$$S(\omega) = 2\beta \frac{(i_o - i_{sc})^2}{i_o^2} \delta(\omega) + 4\beta \left[ \frac{(i_o - i_{sc})i_{sc}}{i_o^2} \right] \frac{e^{-\bar{m}}}{1 - e^{-\bar{m}}} \sum_{j=1}^{+\infty} \frac{\bar{m}^j}{j!} S_j(\omega) + 2\beta \left( \frac{i_{sc}}{i_o} \right)^2 \frac{e^{-2\bar{m}}}{(1 - e^{-\bar{m}})^2} \sum_{j=1}^{+\infty} \frac{\bar{m}^j}{j!} S_j(\omega) (2^j - 2) \tag{9}$$

where

$$S_j(\omega) = \frac{\sqrt{12\xi} a}{\langle V^2 \rangle^{\frac{1}{2}}} \frac{1}{\pi} \left\{ \left( \frac{W(\omega)}{2} \right)^{j-\frac{1}{2}} \frac{\pi^{\frac{1}{2}}}{\Gamma(j)} K_{j-\frac{1}{2}}(W(\omega)) \right\} \tag{10}$$

and  $\Gamma(j)$  is a gamma function,  $K_j$  is a modified Bessel function of the second kind and

$$W(\omega) \equiv \frac{\sqrt{12\xi} a}{\langle V^2 \rangle^{\frac{1}{2}}} \omega. \tag{11}$$

Finally,  $\langle V^2 \rangle^{\frac{1}{2}}$  is the RMS velocity of the moving particles (i.e., the blood RMS velocity).

Equation (9) represents the general model and holds for any optode spacing (or tissue volume). In fact, the model represented by equation (9) has been simply derived without introducing any simplification directly or indirectly related to the measurement volume size in the derivation steps.

Now, for practical reasons it is necessary to express  $i_0$  and  $i_{sc}$  as a function of parameters that can be derived experimentally. Thus, by using equation (6),  $i_{sc}$  may be rewritten as

$$i_{sc} = i_0(1 - e^{-\bar{m}}) \quad (12)$$

where  $P_0 = e^{-\bar{m}}$  is the probability that a photon has no collisions with a moving particle. Using equation (12) and the fact that for the present applications we can consider  $\omega > 0$ , equation (9) can be rewritten as

$$S(\omega) = 2\beta e^{-2\bar{m}} \sum_{j=1}^{+\infty} \frac{(2\bar{m})^j}{j!} S_j(\omega). \quad (13)$$

The validity of the assumptions used to derive the model and the values of the parameters have already been demonstrated elsewhere (Bonner *et al* 1981, Bonner and Nossal 1981).

As an example, the first three terms of  $S_j(\omega)$  may be written as

$$S_1(\omega) = \frac{\sqrt{12\xi}a}{\langle V^2 \rangle^{\frac{1}{2}}} \frac{1}{2} e^{-W(\omega)} \quad (14)$$

$$S_2(\omega) = \frac{\sqrt{12\xi}a}{\langle V^2 \rangle^{\frac{1}{2}}} \frac{1}{4} (W(\omega) + 1) e^{-W(\omega)} \quad (15)$$

$$S_3(\omega) = \frac{\sqrt{12\xi}a}{\langle V^2 \rangle^{\frac{1}{2}}} \frac{1}{16} (W(\omega)^2 + 3W(\omega) + 3) e^{-W(\omega)}. \quad (16)$$

In a more general form  $S_j(\omega)$  becomes

$$S_j(\omega) = \frac{\sqrt{12\xi}a}{\langle V^2 \rangle^{\frac{1}{2}}} \frac{e^{-W(\omega)}}{2^j \Gamma(j)} \left\{ W(\omega)^{j-1} + \sum_{k=1}^{j-1} \left( \frac{\prod_{l=1}^k [4(j - \frac{1}{2})^2 - (2l - 1)^2]}{k! 8^k} W(\omega)^{j-1-k} \right) \right\}. \quad (17)$$

### 2.3. Fitting the model to the experimental data

The fitting procedure was applied to the experimental data points  $P_{LDP}(\omega)$  in the interval  $158 \leq \nu \leq 7967$  Hz. The lower cut-off frequency enables one to neglect the dc component, i.e. the  $i_0^2 \delta(\omega)$  term in equation (3) or 50 Hz interference derived from the instrument whilst the upper cut-off frequency limit represents a practical limitation set by the experimental signal-to-noise ratio (SNR) (see section 3). Even if light shrouding reduces optical interference at the same frequency, the lower cut-off frequency also eliminates the remaining instrumental noise at 100 Hz. Thus, using equations (1), (2) and (3), the model may be generally written in terms of measurable quantities as

$$\hat{P}_{LDP}(\omega) = A^2 \text{dc}^2 \delta(\omega) + \frac{(qBC)A^2 \text{dc}}{\pi} + B^2 C^2 A^2 D(\omega) + A^2 \text{dc}^2 S(\omega) \quad (18)$$

and more simply for practical use:

$$\hat{P}_{LDP}(\omega) \approx A^2 \text{dc}^2 S(\omega) + \text{offset} \quad (158 \leq \nu \leq 7967) \quad (19)$$

where 'offset' is a mean  $D(\omega)$  value taken over an  $\omega$  interval where  $D(\omega)$  is 'flat' (i.e., where  $S(\omega) = 0$ ).

Actually, to compute  $P_{LDP}(\omega)$  it is necessary to multiply the measured ac voltage (in the time domain) by a Hanning window ( $h(t)$ ). This is introduced to reduce side lobe effects on the spectrum. The inclusion in the model of this windowing procedure (in this case in the

frequency domain) implies the convolution (\*) of the model with the power spectrum of the Hanning window ( $|\tilde{h}(\omega)|^2$ ):

$$\hat{P}_{LDP}(\omega) * |\tilde{h}(\omega)|^2 = (A^2 \text{dc}^2 S(\omega) + \text{offset}) * |\tilde{h}(\omega)|^2 \tag{20}$$

where  $\tilde{h}(\omega)$  represents the Fourier transform. In practice, in human skeletal muscle at rest, for  $\nu \geq 8000$  Hz,  $P_{LDP}(\omega)$  becomes flat and the offset may be computed by taking the mean of  $P_{LDP}(\omega)$  over the interval  $8000 \leq \nu \leq 10000$  Hz. In this manner the offset will appear as a known parameter in the fitting procedure (see section 4). In the interval  $8000 \leq \nu \leq 10000$ ,  $\tilde{h}(\omega)$  has no effect on the offset (it is equivalent to multiplying by 1), thus, it corresponds to the real value without windowing. As previously observed, using equation (19) or (20) makes no significant difference to the estimated parameters. For this reason, only equation (19) will be considered from now on.

The last necessary step is to express  $S(\omega)$  for a finite number of terms (equation (13)). The necessary number of terms to be utilized will be discussed in section 3.1. For the sake of clarity, the following is defined:

$$v \equiv \frac{\langle V^2 \rangle^{\frac{1}{2}}}{\sqrt{12\xi a}} \tag{21}$$

The variables  $\bar{m}$ ,  $v$  and the instrumental factor  $\beta$  are the unknown parameters to be found from the model. It is worth mentioning that  $v$  is proportional to the RMS velocity of the moving particles (the blood RMS velocity) and that equation (13) will be no longer explicitly dependent on  $\xi$  or  $a$ .

In conclusion, the model parameters  $\bar{m}$ ,  $v$  and  $\beta$  are obtained by minimizing the squared difference between the measured data,  $P_{LDP}(\omega)$ , and the model function,  $\hat{P}_{LDP}(\omega)$  (equation (19)), using a nonlinear least-squares algorithm (Levenberg Marquardt). In vector notation the functional to be minimized is

$$\text{Min}_{\bar{m}, v, \beta} \left( \frac{1}{2} \| P_{LDP} - \hat{P}_{LDP} \|_2^2 \right) \tag{22}$$

where  $\| \cdot \|_2$  is the usual  $L_2$  norm. Constraints on  $\bar{m}$ ,  $v$  and  $\beta$  may be used to improve the computation speed and to reduce the chance of being trapped in local minima. For example, the constraints  $\bar{m} \geq 0$ ,  $v \geq 0$  and  $0 < \beta < 1$  can be routinely used. The fitting software was written in Matlab 6 language (The MathWorks Inc., Natick, MA, USA).

#### 2.4. Classical approximation for very small tissue volumes

When studying tissue volumes  $< 1 \text{ mm}^3$ , as is the case for skin measurements, it is common to compute the approximation ( $\bar{m} \ll 1$ ) of the first moment of  $S(\omega)$  because the first moment is considered to be proportional to  $\bar{m} \langle V^2 \rangle^{\frac{1}{2}}$ , i.e. proportional to the tissue blood perfusion (Bonner *et al* 1981, Bonner and Nossal 1981). Thus, in the present case by calculating the first moment of equations (10), (13) and (19) one obtains

$$\int_0^{+\infty} \omega \hat{P}_{LDP}(\omega) d\omega = A^2 \text{dc}^2 \int_0^{+\infty} \omega S(\omega) d\omega = A^2 \text{dc}^2 2\beta e^{-2\bar{m}} \int_0^{+\infty} \omega \sum_{j=1}^{+\infty} \frac{(2\bar{m})^j}{j!} S_j(\omega) d\omega. \tag{23}$$

By expanding equation (23) in a Taylor series for  $\bar{m} \ll 1$ :

$$\int_0^{+\infty} \omega \hat{P}_{LDP}(\omega) d\omega \cong A^2 \text{dc}^2 2\beta \frac{\langle V^2 \rangle^{\frac{1}{2}}}{\sqrt{12\xi a}} \bar{m}. \tag{24}$$

The first moment is proportional to the blood flow represented here by  $\langle V^2 \rangle^{\frac{1}{2}} \bar{m}$ . It should be noted that, equation (24) is valid only when the offset has been subtracted from the acquired spectrum.

Following the same procedure it is possible also to compute the zero moment of  $S(\omega)$  for  $\bar{m} \ll 1$ . This usually gives a value proportional to  $\bar{m}$ , i.e. proportional to the tissue blood density. One can obtain

$$\int_0^{+\infty} \hat{P}_{\text{LDP}}(\omega) d\omega \cong A^2 dc^2 2\beta \bar{m}. \quad (25)$$

The calculation of the moments represents the ‘standard’ approach utilized by the existing LDP instruments designed for skin blood perfusion measurements. This approach will be compared with the method proposed in the present work.

### 2.5. Definition of the series truncation order

When dealing with real calculations it is necessary to define a finite maximal value for the index  $j$  appearing in equation (13), i.e.,  $S(\omega)$  is expressed as a truncated series and it is necessary to determine the number of terms needed before any additional terms have a negligible effect on  $S(\omega)$  value. A way of obtaining this is to simulate  $S(\omega)$  numerically for a finite number of series terms and hence determine the necessary number of terms. The truncation limit depends on the possible  $\langle V^2 \rangle^{\frac{1}{2}}$  and  $\bar{m}$  range of variation dictated by the physiological tissue conditions or instrumental conditions. For example,  $\bar{m}$  typically increases with LDP optode spacing. For this reason we have developed a Matlab software to study the convergence of the series (equation (13)) as a function of  $\langle V^2 \rangle^{\frac{1}{2}}$  and  $\bar{m}$ . This software should allow one to identify a suitable  $j$  for any kind of instrumental or physiological condition. A compiled version of the software working on Windows 2000 may be freely obtained from the authors.

### 2.6. Precision of the fitted parameters: a Monte Carlo simulation

*Simulation 1.* To estimate the robustness of the model a series of synthetic experimental spectra with 1024 points (zero to Nyquist frequency),  $A^2 dc^2 S(\omega_n)$  ( $n = 1, \dots, 1024$  and  $158 \leq \omega_n/2\pi \leq 7967$ ), were generated using equations (13) and (17). This corresponds to the experimental data without any offset and noise. The series expressing  $S(\omega_n)$  was developed to the 80th order, i.e.,  $j = 1, \dots, 80$  (see section 3). One hundred ( $\langle V^2 \rangle^{\frac{1}{2}}, \bar{m}, \beta$ ) triplets were randomly sampled in a physiological range (and  $v$  was subsequently calculated using equation (21)). Values for  $\langle V^2 \rangle^{\frac{1}{2}}$  were uniformly chosen in the interval  $[0, 10]$  mm s<sup>-1</sup>,  $\bar{m}$  in the interval  $[0, 25]$  and  $\beta$  in the interval  $[0.004, 0.008]$ . The values for  $A$  and  $dc$  were 900 and  $\frac{14}{30}$  V, respectively. These values, for example, represent a typical muscle in resting conditions with an interoptode spacing of 2 cm (the signal being collected with a bundle of  $4 \times 400/430$   $\mu\text{m}$  fibres as in our instrument). The  $A$  and  $dc$  values (and actually also  $\beta$ ) appear in this case just as scaling factors and do not influence the simulation for the purposes of this test. One ( $\langle V^2 \rangle^{\frac{1}{2}}, \bar{m}, \beta$ ) triplet allows one to generate one 1024-point  $S(\omega_n)$  ( $n = 0, \dots, 1023$ ) experimental dataset. Normally distributed random noise (see section 3 on human skeletal muscle), with a mean of zero and a standard deviation of 0.002 V<sup>2</sup> s, was added to each obtained  $A^2 dc^2 S(\omega_n)$  ( $n = 0, \dots, 1023$ ) dataset. To give an intuitive idea of the noise value one can consider the highest values of  $A^2 dc^2 S(\omega_n)$  (i.e. at the lower frequency, 158 Hz) and calculate the signal-to-noise ratio (SNR) for  $\langle V^2 \rangle^{\frac{1}{2}} = 5$  mm s<sup>-1</sup>,  $\bar{m} = 5$  and  $\beta = 0.006$ , respectively. This gives an SNR of  $\sim 6.17$ . This SNR depends on  $\langle V^2 \rangle^{\frac{1}{2}}, \bar{m}$  as in the case of real experiments. With one ( $\langle V^2 \rangle^{\frac{1}{2}}, \bar{m}, \beta$ ) triplet, forty  $A^2 dc^2 S(\omega_n)$  ( $n = 0, \dots, 1023$ )

datasets with different random noise were obtained. This results in a total of  $40 \times 100 = 4000$  synthetic experimental datasets. The 4000 synthetic datasets were fitted using the fitting procedure described above and the computed parameters  $\langle \hat{V}^2 \rangle^{\frac{1}{2}}$ ,  $\hat{m}$  and  $\hat{\beta}$  were compared to the true  $\langle V^2 \rangle^{\frac{1}{2}}$ ,  $\bar{m}$  and  $\beta$ . The chosen values of the parameters are typical of those found in the *in vivo* measurements (see below). These values have also been used for other mathematical simulations or phantom building (see, e.g., Bonner and Nossal 1981, Obeid 1993).

*Simulation 2.* The effect of the noise intensity on the computed  $\langle \hat{V}^2 \rangle^{\frac{1}{2}}$ ,  $\hat{m}$  and  $\hat{\beta}$  were studied as in ‘simulation 1’ but in this case with a noise standard deviation of  $0.020 V^2$  s. For this purpose, the same batch of  $(\langle V^2 \rangle^{\frac{1}{2}}, \bar{m}, \beta)$  triplets as in ‘simulation 1’ was utilized. In this case the SNR is  $\sim 61.75$ .

### 2.7. Comparison between the ‘classical’ and the new algorithms

A set of spectra were generated for different  $\langle V^2 \rangle^{\frac{1}{2}}$  and  $\bar{m}$  values (see section 3). The parameter  $\beta$  was set to 0.006 ( $\beta$  acts here just as a scaling factor). The zero and first moments of these spectra were computed in the interval 158 to 7967 Hz. The zero and first moment values obtained were then compared with the theoretical values predicted by equations (24) and (25). This has allowed us to theoretically study the range of validity of the ‘classical’ algorithms. Since this simulation might be of general interest to other workers building LDP instruments, it has also been included in the software available to the reader mentioned in section 2.5.

### 2.8. Experimental examples: measurements on phantom

A liquid phantom (Lipovenös, Fresenius Kabi AG, CH; 20%) was used to show the behaviour of  $\bar{m}$  and  $\langle V^2 \rangle^{\frac{1}{2}}$  as a function of the moving particle concentration and interoptode distance.

*Example a.* In the first experiment, the optodes were placed in the phantom solution at 5% concentration. Two series of measurements were performed with interoptode spacings of 1.0 and 1.5 cm. The acquisition time for one averaged spectrum was 0.5 s. Each full spectrum has 1024 points. For each spacing the spectra were acquired for 3 min. To improve the SNR, especially for large optode distance, a sliding rectangular window (average of 16 spectra) was applied.

*Example b.* In the second experiment, the optodes were placed at 1.0 cm distance and the measurements were performed with the same acquisition parameters as in example a but for different phantom concentrations (between 4 and 20%).

### 2.9. Experimental examples: measurements on human forearm

As an example of how it is possible to apply the theory developed in the present study, two different types of experimental measurements have been performed on the human forearm allowing us to show how to estimate the noise figure and the typical  $\bar{m}$  and  $\langle V^2 \rangle^{\frac{1}{2}}$  values.

*Example a.* In the first case the optodes were placed along the *brachioradialis* muscle. The arm and the optodes were covered with a black cloth to eliminate any possible influence of the laboratory illumination on the measurements (the NIR component of a normal tungsten lamp may introduce 50 Hz and 100 Hz noise in the measured spectrum). Three series of measurements were performed with interoptode spacings of 1.5, 2 and 2.5 cm. The acquisition time for one averaged spectrum was 0.5 s. Each full spectrum has 1024 points (i.e., the second half of the 2048-point spectrum is redundant). For each spacing the spectra were acquired

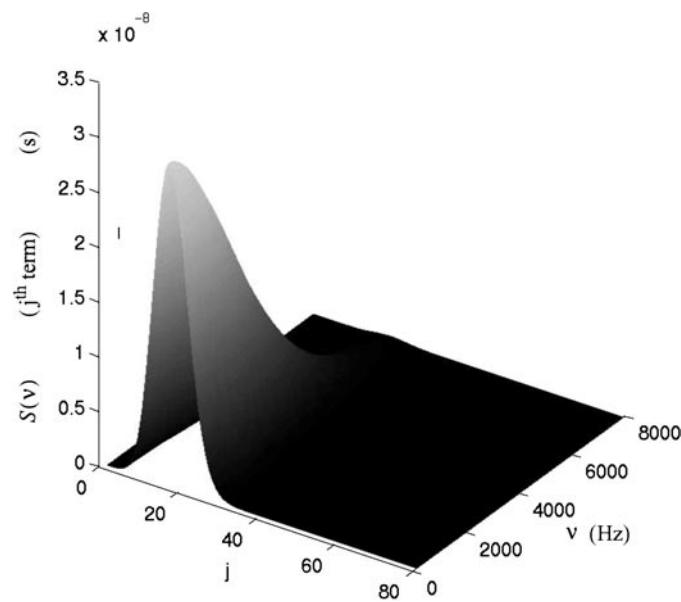


**Figure 2.** Values of the  $j$ th terms of the series  $S(\omega)$  (equation (13)) as a function of  $j$  and  $\omega/2\pi$  for  $\langle V^2 \rangle^{\frac{1}{2}} = 8 \text{ mm s}^{-1}$ ,  $\bar{m} = 9$  and  $\beta = 0.006$ .

for 1 min. To improve the SNR, especially for large optode distance, a sliding rectangular window (average of 16 spectra) was applied.

*Example b.* To study the stability of the measurements, a series of six acquisitions were performed over a  $\sim 2.5$  h period. Each series consisted of a 3 min spectra acquisition with the instrument parameter set as in example a. The interoptode distance in this case was 2 cm.

#### 2.10. Domain of validity for large optode spacing: example of human forearm

*Example c.* To induce  $\bar{m}$  and  $\langle V^2 \rangle^{\frac{1}{2}}$  changes and to show a possible physiological range for  $\bar{m}$  and  $\langle V^2 \rangle^{\frac{1}{2}}$  an ischaemia–reperfusion protocol was utilized. In this case the optodes were positioned along the hand flexor muscles with an interoptode spacing of either 1.5 or 2 cm. The sampling time for one averaged spectrum was 0.5 s and the total acquisition time 3 min. Also in this case a sliding window was applied over 16 spectra. The protocol consisted of 1 min control, 1 min arterial occlusion and 1 min recovery. Arterial occlusion was obtained by inflating a cuff, placed around the arm, at suprasystolic pressure.

### 3. Results

#### 3.1. Definition of the series truncation order

Figure 2 presents an example, for  $\langle V^2 \rangle^{\frac{1}{2}} = 8 \text{ mm s}^{-1}$  and  $\bar{m} = 9$ , showing the convergence of the series terms composing equation (13). On the horizontal axis one finds the spectrum frequency  $\nu$  and the index  $j$  of the  $S(2\pi\nu)$   $j$ th series term (equation (13)). On the vertical axis is reported the value of the  $j$ th term of  $S(2\pi\nu)$ . One can see that in this case the series converges for a  $j$  less than 80, the value that was generally chosen for the examples presented

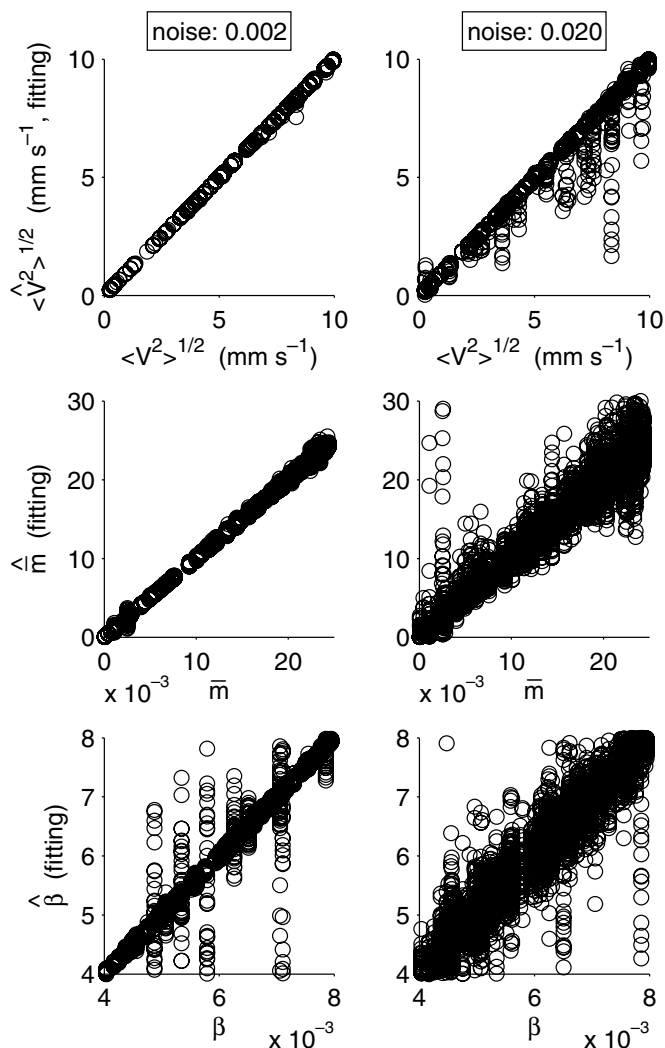


**Figure 3.** Results of the Monte Carlo simulation. Parameters with  $\wedge$  correspond to the estimated values obtained by the fitting procedure (see section 3.2).

in the present work. This also holds for higher  $\langle V^2 \rangle^{1/2}$  and  $\bar{m}$  values which are not shown here. In practice, if one fits the data obtained on the human arm (see below) with 80 or 90 terms, there is no difference (up to two decimal points for  $\langle V^2 \rangle^{1/2}$ ) in the resulting  $\langle V^2 \rangle^{1/2}$  and  $\bar{m}$  values.

*3.2. Precision of the fitted parameters: a Monte Carlo simulation*

Figure 3 shows the stability of the fitting procedure on the synthetic data generated from the model (equation (13)). The estimated  $\langle \hat{V}^2 \rangle^{1/2}$ ,  $\hat{m}$  and  $\hat{\beta}$  parameter values are reported as a function of  $\langle V^2 \rangle^{1/2}$ ,  $\bar{m}$  and  $\beta$ . The left panel of figures represents spectra with a noise standard deviation of 0.002 while in the right panel the noise is equal to 0.020. It appears in both cases that  $\langle V^2 \rangle^{1/2}$  is the parameter least sensitive to noise. At the noise level of 0.002  $V^2$  s the regression coefficients for  $\langle \hat{V}^2 \rangle^{1/2}$ ,  $\hat{m}$  and  $\hat{\beta}$  are 1.00, 1.00 and 0.70, respectively. At the noise

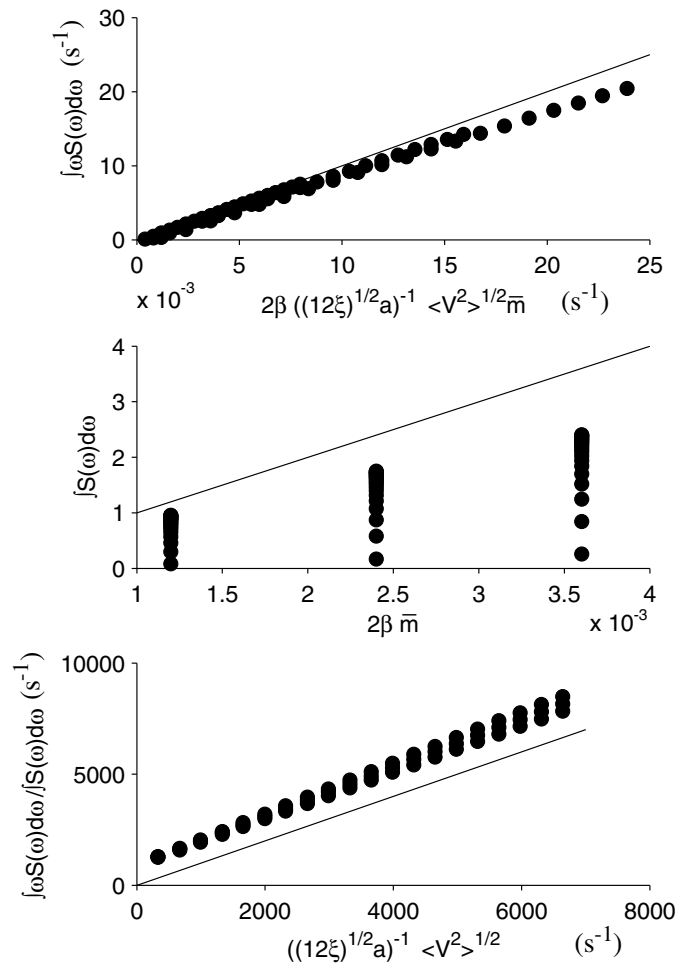


**Figure 4.** First and second moments of the spectra, for different  $\bar{m}$  and  $\langle V^2 \rangle^{1/2}$ , calculated over the frequency interval  $158 \leq \omega_n/2\pi \leq 7967$  and compared with the actual theoretical values (see section 2.7). The parameter values for  $\langle V^2 \rangle^{1/2}$  varied from 1 to 20 in steps of 1 mm s<sup>-1</sup> and  $\bar{m}$  was equal to 0.1, 0.2 and 0.3.

level of 0.020 V<sup>2</sup> s the regression coefficients for  $\langle \hat{V}^2 \rangle^{1/2}$ ,  $\hat{m}$  and  $\hat{\beta}$  are 0.99, 0.93 and 0.19, respectively.

3.3. Comparison between the ‘classical’ and the present algorithms

In figure 4 are shown the zero moment, the first moment and their ratio, for spectra generated from equation (13), as a function of the theoretical value predicted by equations (22) and (23). It can be seen that the analytical expression of the ratio, i.e.,  $\int \omega S(\omega) d\omega / \int S(\omega) d\omega$ , is independent of  $\bar{m}$  and can be considered as an RMS velocity term. The continuous lines represent the identity lines. The values of the different simulation parameters were:  $\langle V^2 \rangle^{1/2}$  from 1 to 20 in steps of 1 mm s<sup>-1</sup> and  $\bar{m}$  equal to 0.1, 0.2 and 0.3. All the combinations of  $\langle V^2 \rangle^{1/2}$  and  $\bar{m}$  were utilized. It appears from the top figure that the first moment, usually considered as ‘flux’, reproduces fairly well the  $2\beta((12\xi)^{1/2}a)^{-1}\langle V^2 \rangle^{1/2}\bar{m}$  data to be predicted for

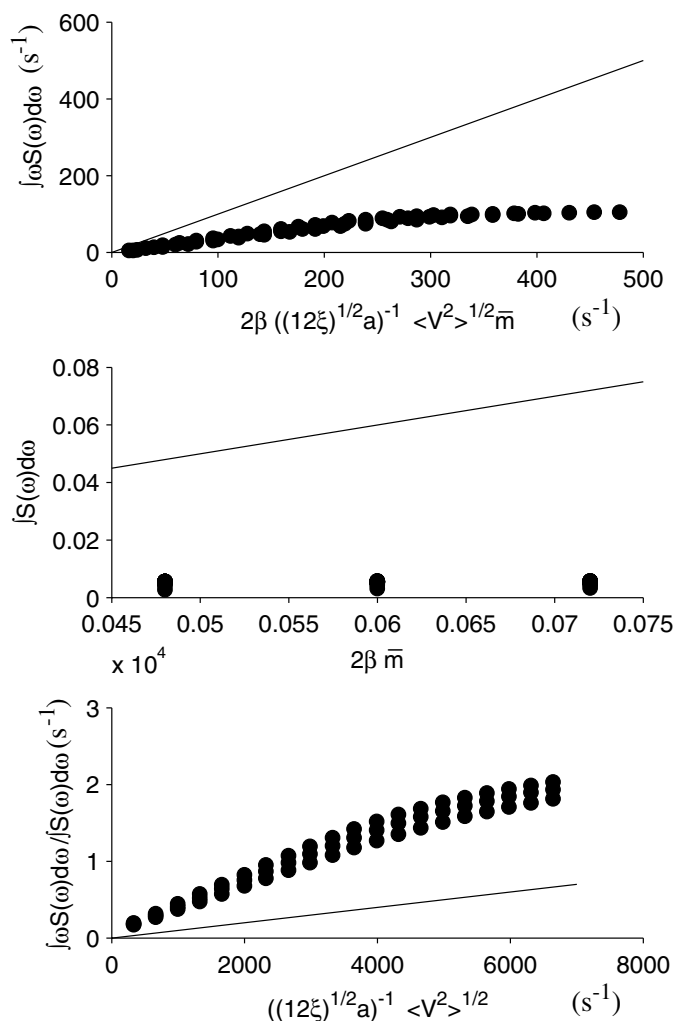


**Figure 5.** First and second moments of the spectra, for different  $\bar{m}$  and  $\langle V^2 \rangle^{1/2}$ , calculated over the frequency interval  $158 \leq \omega_n/2\pi \leq 7967$  and compared with the actual theoretical values (see section 3.3). The parameter values for  $\langle V^2 \rangle^{1/2}$  varied from 1 to 20 in steps of 1 mm s<sup>-1</sup>, as in figure 4, but  $\bar{m}$  was equal to 4.0, 5.0 and 6.0.

the proposed  $\bar{m}$  values. Also the ratio between the moments (bottom figure) has a reasonably linear relationship with the RMS velocity term  $((12\xi)^{1/2}a)^{-1}\langle V^2 \rangle^{1/2}$ . Even with increasing  $\langle V^2 \rangle^{1/2}$  the precision depends more and more on  $\bar{m}$  (the vertical scatter). The ratio data show a good linear correlation in the whole range but also shows a methodological offset. The least precise prediction is given by the zero moment describing the  $2\beta\bar{m}$  term. It can be seen in this case (middle figure) that the zero moment strongly depends on the  $\langle V^2 \rangle^{1/2}$  and  $\bar{m}$  magnitudes (the vertical scatter).

In figure 5 the results of the same simulation are given but with  $\bar{m}$  equal to 4.0, 5.0 and 6.0. The top figure shows that the classical model clearly breaks down for  $\bar{m}$  values larger than 1 and that the estimated ‘perfusion’ values are no longer linear. The same problem holds for the zero moment and the ratio between the moments.

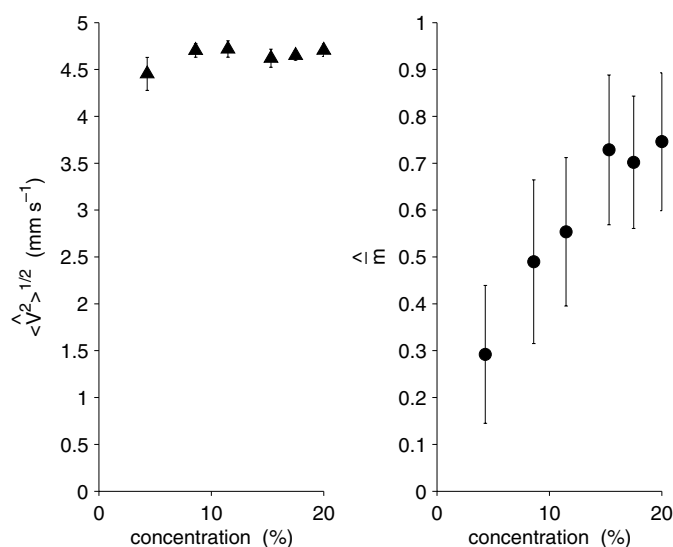


**Figure 6.** RMS velocity,  $\langle \hat{V}^2 \rangle^{1/2}$  (triangles), and  $\bar{m}$  values (circles) as a function of liquid phantom concentration with an optode spacing of 1 cm. The vertical bars represent the standard deviation.

### 3.4. Experimental examples: measurements on phantom

*Example a.* The  $\langle V^2 \rangle^{1/2}$  and  $\bar{m}$  values, were  $3.88 \pm 0.41$  mm s<sup>-1</sup> and  $0.36 \pm 0.23$  for 1.5 cm spacing, and  $4.05 \pm 0.11$  mm s<sup>-1</sup> and  $0.28 \pm 0.13$  for 1.0 cm spacing, respectively. The values correspond to the mean and standard deviation over all the measurements taken during 3 min (see section 2).

*Example b.* Figure 6 shows the behaviour of  $\langle V^2 \rangle^{1/2}$  and  $\bar{m}$  as a function of the solution concentration of the phantom. The RMS velocity  $\langle V^2 \rangle^{1/2}$  does not depend on the concentration but  $\bar{m}$  decreases for decreasing concentration as one might expect.

### 3.5. Experimental examples: measurements on human forearm

*Example a.* The normality of the noise (over the interval  $8000 \leq \nu \leq 10000$  Hz) was tested on each spectrum taken at 1.5, 2 and 2.5 cm for a total of  $357 \times 3 = 1071$  spectra. To do this, the single sample Lilliefors hypothesis test of composite normality was used. The significance level was set to  $p < 0.05$ . It was found that 89.92, 92.72 and 80.67% of the spectra had normally distributed noise for optode spacings of 1.5, 2 and 2.5 cm, respectively. This is the reason why normal noise has been utilized for the simulations.

*Example b.* Figure 7 shows six repeated measurements performed on the same subject over a period of about 2.5 h. It appears that  $\langle \hat{V}^2 \rangle^{1/2}$  is the most stable parameter.

### 3.6. Domain of validity for large optode spacing: example of human forearm

*Example c.* In figure 8 data for  $\langle \hat{V}^2 \rangle^{1/2}$  at 1.5 cm interoptode spacing are shown as a function of time during the ischaemia–reperfusion protocol. The black bar represents the ischaemic period. The typical post-ischaemic hyperaemia and increase in tissue blood perfusion can be clearly detected. The increase in blood RMS velocity is in fact due to vasodilation (at the end of the black bar).

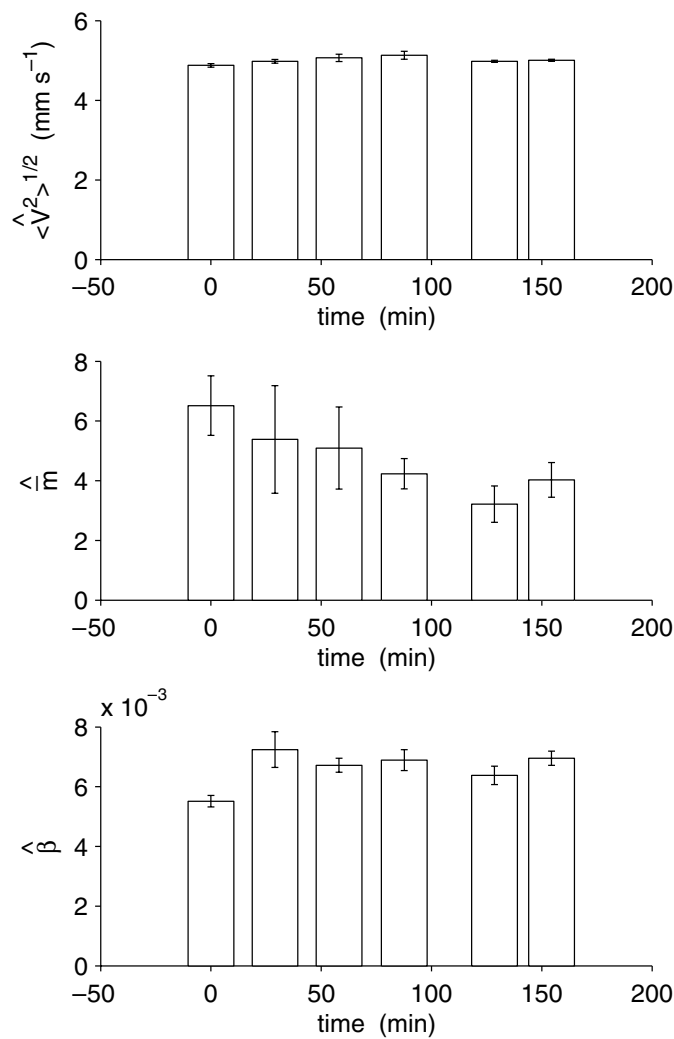


**Figure 7.** Repeated measurements on human brachioradialis muscle to test the stability of the estimated parameters  $\langle \hat{V}^2 \rangle^{1/2}$ ,  $\hat{m}$  and  $\hat{\beta}$ .

The measurements at 2 cm are not shown because during the reperfusion period,  $\hat{m}$  reaches very high values resulting in poor SNR. Moreover, with large  $\hat{m}$  values, the spectra become ‘flat’. However it has been possible to estimate the  $\langle \hat{V}^2 \rangle^{1/2}$  values at rest and during ischaemic periods (at steady state). These were  $9.99 \pm 0.01$  ( $n = 61$ ) and  $5.58 \pm 0.03$  ( $n = 31$ ) mm s<sup>-1</sup> at 1.5 cm and  $5.18 \pm 0.01$  ( $n = 81$ ) and  $2.54 \pm 0.09$  ( $n = 26$ ) mm s<sup>-1</sup> at 2 cm. In this case  $\hat{m}$  values remain below 4 and the fitting procedure is reliable. The values at steady state during ischaemic periods correspond to the so-called ‘biological zero’.

#### 4. Discussion

With a few exceptions, the majority of the LDP instruments found in the market today are built for measurements at very short optode spacing, i.e.  $\bar{m} \ll 1$  and relatively low  $\langle V^2 \rangle^{1/2}$

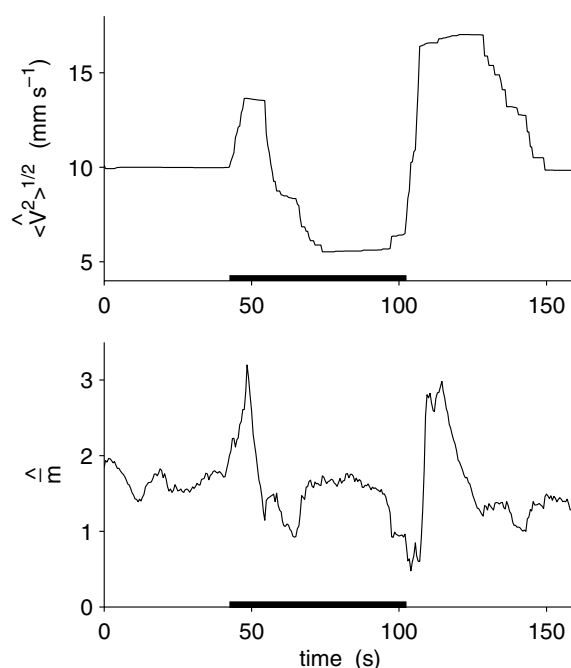


**Figure 8.** Human brachioradialis muscle blood RMS velocity,  $\langle \hat{V}^2 \rangle^{1/2}$ , during an ischaemia-perfusion protocol. The black bar represents the ischaemic period.

(Nilsson 1984, Leahy *et al* 1999). In this paper an algorithm was derived allowing one to obtain blood RMS velocity,  $\langle \hat{V}^2 \rangle^{1/2}$ , using a near-infrared laser Doppler instrument, for any values of  $\bar{m}$  and  $\langle V^2 \rangle^{1/2}$ . Our Monte Carlo simulation showed that the error in the estimated parameters depends strongly on the noise level (figure 3) but  $\langle \hat{V}^2 \rangle^{1/2}$  is reasonably stable for the noise level obtainable with the present LDP instruments (e.g., left panel of figure 3). However, to obtain reliable results it is necessary to previously define the minimum number of terms to include in the series describing the present model (equation (13)). This may be done with the approach presented in figure 2. In fact, the larger the  $\langle \hat{V}^2 \rangle^{1/2}$  and  $\hat{m}$  values, the higher the number of series terms must be. As we have seen, the  $\langle \hat{V}^2 \rangle^{1/2}$  and  $\hat{m}$  magnitude may depend on instrumental factors (e.g., the interoptode spacing) or physiological factors (e.g., blood volume, hyperaemic reaction, etc). It is appropriate to overestimate the number of terms, but this will inevitably increase the computation time considerably.

When dealing with measurements on small tissue volumes, it is always possible to use the ‘classical’ approximation, i.e.  $\bar{m} \ll 1$  in equations (24) and (25). It would be interesting to introduce explicitly the parameters  $A$ ,  $dc$ ,  $\xi$ ,  $\beta$  and  $a$  to obtain absolute ‘flux’, i.e.  $\langle \hat{V}^2 \rangle^{1/2} \hat{m}$  (see, e.g., figure 4, top) as is the case for the fitting method presented in this work. Unfortunately,  $\beta$  remains unknown, depends on instrumental factors and it seems to vary during the experiments. If one wants to use this approach, further studies on the behaviour of  $\beta$  are necessary. A scaled absolute value of  $\langle \hat{V}^2 \rangle^{1/2}$  can be estimated using the ratio of the first to zero moments where the  $\beta$  term cancels out. The remaining problem observed in this study is the presence of a methodological error shifting the  $\langle \hat{V}^2 \rangle^{1/2}$  curves to higher values. This overestimation of the  $\langle \hat{V}^2 \rangle^{1/2}$  values is due to the fact that the curve is integrated only over a limited  $\nu$  range ( $158 \leq \nu \leq 7967$ ) and not over 0 to  $+\infty$  as it should be (see equation (24)).

Thus, to improve the precision, the solution would be to build instruments allowing one to use frequencies as near as possible to  $\nu = 0$ . It has been demonstrated experimentally (Nilsson 1984) that the first moment starts to deviate from the identity line for high  $\langle \hat{V}^2 \rangle^{\frac{1}{2}}$  values and that actually the measurement does not depend too much on  $\hat{m}$ . This is exactly what we observe in figure 4 (top). Nilsson (1984) has proposed an experimental method to ‘linearize’ the ‘flux’ values allowing the LDP to work for larger  $\langle \hat{V}^2 \rangle^{\frac{1}{2}}$  values. The kind of simulation presented in figure 4 (top) might be utilized to correct the ‘flux’ values without the need for experimental data and with the advantage of being able to study an undetermined large number of experimental parameter situations. Of course, if one directly fits the model, represented by equation (13), to the spectra, all the problems appearing above disappear and the ‘classical’ LDP should be able to give absolute values. For large  $\bar{m}$  values this is the only remaining solution because the ‘classical’ approach is no longer valid (see figure 5). As noted by Liebert *et al* (1999), several methods have been proposed for calibrating LDP instruments. Among others, some are based on tissue preparations (Ahn *et al* 1987), flow models (Nilsson *et al* 1980, Obeid 1993), rotating discs (Smits *et al* 1986), Brownian motion of scattering particles (Fairs 1988, Liebert *et al* 1995) and controlled movement of scattering particles (Steenbergen and DeMul 1998). These approaches will of course remain extremely useful because they will allow us to further test the present algorithm and/or its future potential improvements. However, neither of these calibration approaches nor the present model can guarantee the quality and the linearity of the LDP instrument itself. This should possibly be checked by other methods before any calibration or measurement procedure (see, e.g., Liebert *et al* 1999).

Returning to the present new approach, in figure 7 it has been shown that the  $\langle \hat{V}^2 \rangle^{\frac{1}{2}}$  measurements are stable over time. The  $\langle \hat{V}^2 \rangle^{\frac{1}{2}}$  values depend on the interoptode spacing. This can be explained because  $\langle \hat{V}^2 \rangle^{\frac{1}{2}}$  depends on at least two factors: the ‘biological zero’ value (included in  $\langle \hat{V}^2 \rangle^{\frac{1}{2}}$ ) and the morphological structure of the investigated tissue volume. In the case of the forearm, the adipose tissue thickness is no longer negligible for an optode spacing larger than 1.5 cm (Binzoni *et al* 1998) and a different fat/muscle volume ratio may influence  $\langle \hat{V}^2 \rangle^{\frac{1}{2}}$  (different vascularization, metabolism, etc). This problem has to be studied further.

At this point, before discussing the ischaemia–reperfusion example, it is interesting to understand intuitively what happens when  $\bar{m}$  becomes large. The parameter  $\bar{m}$  appears as a general amplitude factor, in the exponential function  $e^{-2\bar{m}}$  found in the model (equation (13)) and this exponential function represents the probability that a photon has not interacted with a moving particle. If  $\bar{m}$  becomes large, this probability goes to zero. The present LDP instrument is based on heterodyne detection and the reference beam is given by the non-Doppler-shifted photons (no phase shift). This means that if  $\bar{m}$  becomes large, the reference light beam intensity becomes negligible and the spectrum ‘flattens’ (i.e., no signal). Thus, the present model is no longer useful for a large  $\bar{m}$ . Typically, this could be the case in the liver where the blood concentration is very high ( $\bar{m}$  increases with blood volume). In fact, in the real tissue, other second-order phenomena also occur. Photons that have scattered off only one moving particle may interact with photons that have scattered twice, and in this way giving rise to a signal. This behaviour appears for large  $\bar{m}$ , modifying in part equation (13). Possible addition of this high-order behaviour to the model, might in the future solve the problem of very large  $\bar{m}$  values. Figures 9(a) and (b) depict the spectra obtained at optode spacings of 1.5 and 2 cm, both displaying Doppler shift characteristics. While the SNR at 1.5 optode spacing is high enough for the estimation of parameters  $\langle \hat{V}^2 \rangle^{\frac{1}{2}}$  and  $\hat{m}$ , the SNR at 2 cm optode spacing is too low for reliable estimation of parameters. At 2.5 and 3 cm (figures 9(c) and (d)), the Doppler signal is too weak and the spectra are determined by low intensity electronic noise. These

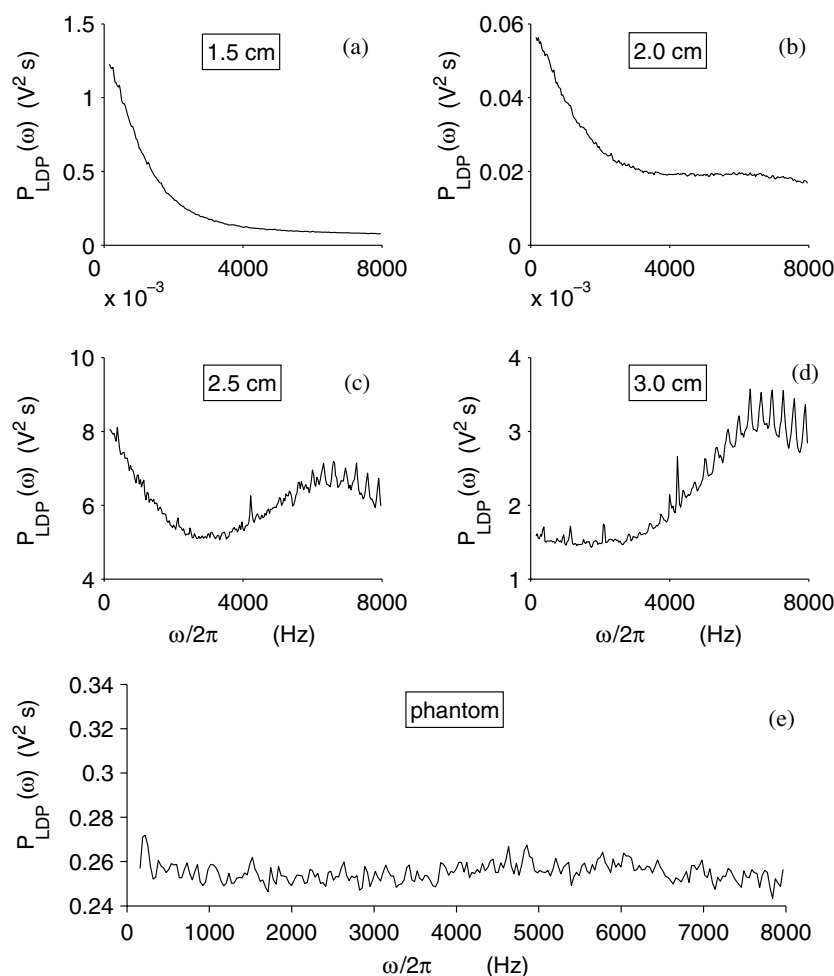


**Figure 9.** Mean of 362 spectra acquired on resting human brachioradialis muscle at 1.5, 2, 2.5 and 3 cm interoptode distances. The bottom figure (e) represents again the mean of 362 spectra but this time acquired on a phantom with no ‘perfusion’ (Delrin phantom). No correction was introduced for the offset.

spectra also cannot be used for parameter estimation. Figure 9(e) shows a flat spectrum which is obtained from a phantom without ‘perfusion’ (Delrin phantom). In conclusion, it is not enough to just modify the hardware to obtain a better SNR, and thus more precise  $\langle \hat{V}^2 \rangle^{\frac{1}{2}}$  and  $\hat{m}$  estimations, but to improve the capability of the model to work at larger optode spacing. At large interoptode distances (e.g., 2.5 cm), second-order phenomena need to be taken into account in the model.

Concerning the precision of the fitting a further point can be highlighted utilizing figure 10 as an example. Figure 10 shows simultaneously the difference between a simulated power spectrum acquired at low RMS velocity (a) and that acquired at high RMS velocity (b). The parameters defining these simulated spectra are:  $5 \text{ mm s}^{-1}$ , 5, 0.006, 1 V, 900,  $0.05 \text{ V}^2$  (figure 9(a)) and  $20 \text{ mm s}^{-1}$ , 5, 0.006, 1 V, 900,  $0.05 \text{ V}^2$  (figure 9(b)) for  $\langle V^2 \rangle^{\frac{1}{2}}$ ,  $m$ ,  $\beta$ ,  $dc$ ,  $A$  and ‘offset’, respectively (note that only  $\langle V^2 \rangle^{\frac{1}{2}}$  changes). The random noise in these examples

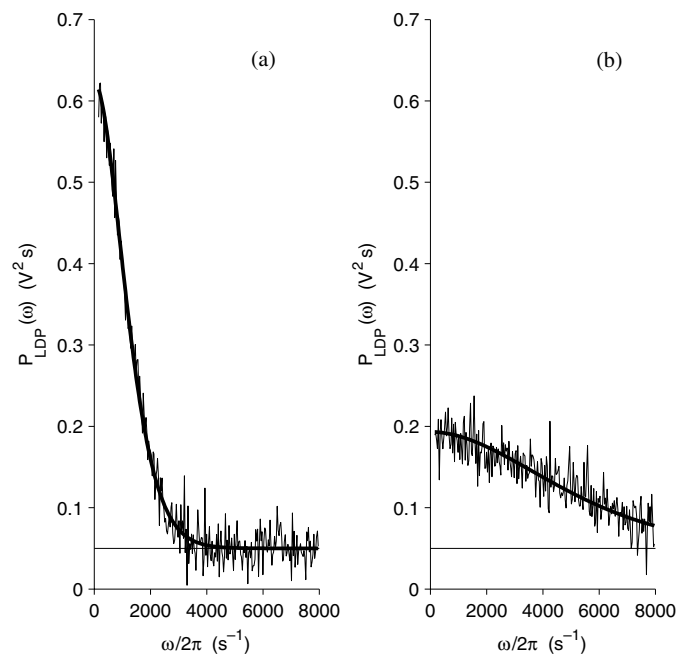


**Figure 10.** Simulated spectra. (a) The values for  $\langle V^2 \rangle^{1/2}$ ,  $\bar{m}$ ,  $\beta$ ,  $dc$ ,  $A$  and 'offset' are  $5 \text{ mm s}^{-1}$ ,  $5$ ,  $0.006$ ,  $1 \text{ V}$ ,  $900$ ,  $0.05 \text{ V}^2 \text{ s}$ , respectively. (b) In this case only  $\langle V^2 \rangle^{1/2}$  is different and has a value of  $20 \text{ mm s}^{-1}$ . The random noise was set to  $0.02 \text{ V}^2 \text{ s}$ . The thick curves represent the fitted model.

was set to  $0.02 \text{ V}^2$ . It appears that for high RMS velocity values the spectrum at low frequency decreases in intensity (compare figures 10(a) and (b)) and the signal has the tendency to disappear into the noise because the curve becomes flat. For high velocities, the curve reaches the baseline level at higher frequencies (outside the figure) than for low velocities. This gives the wrong 'impression' that the offset is shifted towards a higher value (figure 10(b)). The practical consequence of this is that, when analysing a physiological experiment, it is first necessary to evaluate the offset for resting values (e.g., in the case of skeletal muscle) and then these values may be used to correct the remaining spectra during RMS velocity transitions (the influence of  $dc$  on the offset should of course also be taken into account). Figure 10 also helps us to realize that for a very low RMS velocity the spectrum becomes narrow and mainly situated in the lower frequency range. This means that if we want to detect very low RMS velocities it would be necessary to use a lower frequency bound for the frequency fitting range (the spectrum magnitude increases at low frequencies). One should however also ensure that by choosing a lower frequency bound, any  $50 \text{ Hz}$  mains interference or other noise sources will not affect the LDP measurements. In practice, the lowest measurable RMS velocity is the 'biological zero' which has a distinctive spectrum in the frequency chosen here.

The results derived from the ischaemia–reperfusion protocol, and appearing in figure 8, show that blood RMS velocity does not go to zero during ischaemia (tourniquet inflated around the arm). This observation is also seen in skin measurements and it is called the 'biological zero' (Tenland *et al* 1983). This may be explained for example by the fact that the erythrocytes or other particles in the interstitial space may continue to move randomly (Brownian motion)

even without net tissue blood perfusion (Kernick *et al* 1999). Considering that the measured quantity is a ‘root-mean-square’ velocity, velocity contributions in all directions are thus taken into account resulting in a nonzero mean speed. The ‘biological zero’ is usually subtracted from the original signal as an offset (Kernick *et al* 1999). This means that if the ‘biological zero’ changes during an experiment (e.g., during oedema formation), then the interpretation of the data may become difficult. The capability of the present approach to derive  $\langle \hat{V}^2 \rangle^{\frac{1}{2}}$  and  $\hat{m}$  independently together with the possibility of studying tissue volumes larger than a fraction of a millimetre cube, might help us to better understand this phenomenon and this may be a subject for future studies. Figure 8 shows another feature that is probably related to changes in ‘biological zero’. The peak observed in the  $\langle \hat{V}^2 \rangle^{\frac{1}{2}}$  versus time graph during cuff inflation, and the long delay necessary to reach the ‘biological zero’ value, is also observed in skin measurements (Kernick *et al* 1999). This is usually interpreted as a redistribution of the interstitial fluids induced by the cuff pressure. Probably the same phenomenon is present in this study.

Another point that could influence  $\langle \hat{V}^2 \rangle^{\frac{1}{2}}$  values are the parameters  $\xi$  and  $a$ . In practice,  $\langle \hat{V}^2 \rangle^{\frac{1}{2}}$  is evaluated by computing  $v$  and then  $\langle \hat{V}^2 \rangle^{\frac{1}{2}}$  is derived using equation (21). Changes in  $\xi$  and  $a$  values (in a ‘physiological’ range) slightly influence  $\langle \hat{V}^2 \rangle^{\frac{1}{2}}$  (but never reduce it to zero during ischaemia). From the model, it can be seen that  $\hat{m}$  and  $\hat{\beta}$  do not depend on  $\xi$  or  $a$ .

It is to be noted that the present method allows us to find ‘absolute’ RMS velocity values and not relative tissue perfusion (i.e., RMS velocity  $\times$  blood volume) values as in classical LDP instruments for skin measurements. The advantage of this is that even if  $\langle \hat{V}^2 \rangle^{\frac{1}{2}}$  values are not absolute (i.e., once  $\xi$  and  $a$  are fixed at any given value), they can be used to compare between different subjects. This is because  $v$  will be always the same and  $\langle \hat{V}^2 \rangle^{\frac{1}{2}}$  will follow equation (21). In other words, fixing  $\xi$  and  $a$  is equivalent to defining a ‘laboratory RMS velocity standard’ for the instrument.

One further advantage of the proposed method is that unlike other techniques (Kienle 2001) it does not require a knowledge of the optical scattering or absorption parameter of the tissue. This allows one to estimate and compare  $\langle \hat{V}^2 \rangle^{\frac{1}{2}}$  values in the cases where the investigated tissues undergo changes in their optical parameters, as for example during cooling or heating (Binzoni *et al* 1999, Hollis *et al* 2001).

At this point it would be interesting to apply the present approach for real-time measure. Unfortunately, the present software was written using an interpreted language (Matlab) and this makes the computations very slow. Typically, the mean time necessary to evaluate one spectrum (i.e. the values of  $\langle \hat{V}^2 \rangle^{\frac{1}{2}}$ ,  $\hat{m}$  and  $\hat{\beta}$ ) is of the order of  $4.86 \pm 2.60$  s for 80 terms in the series (13). If we reduce the number of series terms to 40 (e.g., for relatively small  $\hat{m}$ ) it takes  $2.08 \pm 1.11$  s. This computational time is too long for real-time applications. However, we can significantly improve the speed by using a compiled and optimized programming language. The use of a faster PC (a Pentium 1 GHz PC is used at present) with a digital signal processor should also reduce the computation time.

## 5. Conclusions

To obtain reliable  $\langle V^2 \rangle^{\frac{1}{2}}$  absolute/comparable values it is essential to have a good SNR, especially when measuring high velocities. This implies the use of a laser having a power higher than that utilized in the present case. The advantage of increasing laser power is the possibility of increasing the interoptode distance resulting in the investigation of larger (and deeper) regions of interest. This may allow for example the transcranial study of the cerebral cortex as is already done with standard NIRS techniques. However, increasing the

interoptode distance too far (e.g., 2.5 cm) may introduce a limit in the validity of the present model because second-order interactions between the photons may appear. It will also be necessary to further reduce electronic noise distortions which also become limiting factors for large optode spacing. A laser wavelength at the haemoglobin isobestic point (800 nm) would also allow monitoring of blood volume changes. To obtain real-time measurements it will be essential to develop faster algorithms or to implement them directly in a digital signal processor. An interesting future development might be the simultaneous utilization of two LDP instruments at two different wavelengths. In this manner the dc data will allow one to compute oxy- and deoxyhaemoglobin concentration changes (as in a conventional NIRS instrument) together with  $\langle V^2 \rangle^{\frac{1}{2}}$ . This would represent a step further towards the fundamental problem of non-invasive oxygen consumption measurements in tissue. To conclude, the present work also proposes a simple approach that may be used to obtain absolute  $\langle V^2 \rangle^{\frac{1}{2}}$  values with 'classical' LDP instruments working at small optode spacing. This approach might allow one to eliminate the need for calibration procedures and solve the problem of data comparison between different instruments.

### Acknowledgments

The authors thank the Swiss National Science Foundation (no 31-58759.99) and the Wellcome Trust for their financial support.

### Appendix

As presented in this paper, a spectrum obtained by an LDP system,  $P_{\text{LDP}}(\omega)$ , may be described as (equation (19)):  $P_{\text{LDP}}(\omega) \approx A^2 \text{dc}^2 S(\omega)$ . We have also shown that the term  $S(\omega)$  may be expressed through the normalized temporal autocorrelation function  $g^{(2)}(\tau)$  (equation (8)) and these represent very general classical results (Cummins and Swinney 1970). Now, the difficulty is to express  $g^{(2)}(\tau)$  for our problem, i.e. the human tissue model. The first step is thus to write  $g^{(2)}(\tau)$  as a function of the intermediate scattering function  $I(\tau)$  of the Doppler-shifted light (equation (4)). The function  $I(\tau)$  must contain all the information necessary to describe a system with multiple scattering.  $I(\tau)$  may be mathematically very complex but, for our purpose, it is necessary to find an explicit mathematical expression for  $I(\tau)$ . The elegant work of Bonner and Nossal (1981) has been to exploit the finding (Sorensen *et al* 1976) that  $I(\tau)$  can be expressed in terms of an intermediate scattering function describing photons that experience only one collision,  $I_1(\tau)$  (equation (5)). This greatly simplifies the expression of  $g^{(2)}(\tau)$ , now in terms of  $I_1(\tau)$ . Bonner and Nossal (1981) were also able to give an explicit and simple form for  $I_1(\tau)$  (equation (7)). In short, this has been done by making the assumption that the moving particles are spherical and that the RMS velocity distribution is normal and by knowing that

$$I_1(\tau) = \frac{\int_{-\pi}^{\pi} \zeta(\vec{Q}(\theta)) \langle e^{i\vec{Q}(\theta)\Delta\vec{R}(\tau)} \rangle \sin \theta \, d\theta}{\int_{-\pi}^{\pi} \zeta(\vec{Q}(\theta)) \sin \theta \, d\theta} \quad (\text{A.1})$$

where  $\zeta(\vec{Q}(\theta))$  is the structure factor of an average scatterer (e.g., sphere in this case) and  $\Delta\vec{R}(\tau)$  is the displacement of the centre of mass of a moving cell during a time  $\tau$ . The expectation is taken over the velocity distribution of the cells. It must be noted that Bonner and Nossal (1981) also demonstrated that this result holds for more general cases because it is a good approximation also for velocity distributions that are not normal (e.g., Newtonian flow in a cylinder) or for non-spherical particle geometry (e.g., biconcave disc). By using the

explicit expression for  $I_1(\tau)$  (equation (7)) one can find the main equations (equations (10) and (13)) for  $S(\omega)$  utilized as a fitting algorithm in the present paper.

## References

- Ahn H, Johansson K, Lundgren O and Nilsson G E 1987 *In vivo* evaluation of signal processors for laser Doppler tissue flowmeters *Med. Biol. Eng. Comput.* **25** 207–11
- Binzoni T, Leung T S, Boggett D and Delpy D 2002 A new near infrared laser-Doppler flowmeter for deep tissue perfusion monitoring *MAGMA* **14** 74–5
- Binzoni T, Quaresima V, Barattelli G, Hiltbrand E, Gurke L, Terrier F, Cerretelli P and Ferrari M 1998 Energy metabolism and interstitial fluid displacement in human gastrocnemius during short ischemic cycles *J. Appl. Physiol.* **85** 1244–51
- Binzoni T, Springett R, Dalton J C and Delpy D 1999 A new combined deep-body-temperature/NIRS probe for noninvasive metabolic measurements on human skeletal muscle *Adv. Exp. Med. Biol.* **471** 623–9
- Boas D A 1996 Diffusive photons probes of structural and dynamical properties of turbid media: theory and biomedical applications *PhD Thesis* University of Philadelphia
- Bonner R F, Clem T R, Bowen P D and Bowman R L 1981 Laser Doppler continuous real-time monitor of pulsatile and mean blood flow in tissue microcirculation *Scattering Techniques Applied to Supramolecular and Nonequilibrium Systems* ed S-H Chen, B Chu and R Nossal (New York: Plenum) pp 685–701
- Bonner R F and Nossal R 1981 Model for laser Doppler measurements of blood flow in tissue *Appl. Opt.* **20** 2097–107
- Cerretelli P and Binzoni T 1997 The contribution of NMR, NIRS and their combination to the functional assessment of human muscle *Int. J. Sports Med.* **18** S270–S279
- Chance B, Cooper C E, Delpy D T and Reynolds E O R (ed) 1997 Near infrared spectroscopy and imaging of living systems *Phil. Trans. R. Soc. B* **352** 643–761
- Cummins H Z and Swinney H L 1970 Light beating spectroscopy *Progress in Optics* ed E Wolf (Amsterdam: North-Holland) vol VIII pp 133–200
- Delpy D T and Cope M 1997 Quantification in tissue near-infrared spectroscopy *Phil. Trans. R. Soc. B* **352** 649–59
- Fairs S L 1988 Observations of a laser Doppler flowmeter output made using a calibration standard *Med. Biol. Eng. Comput.* **26** 404–6
- Hollis V, Binzoni T and Delpy D T 2001 Non-invasive monitoring of brain tissue temperature by near-infrared spectroscopy *Proc. SPIE* **4250** 470–81
- Johnson C S Jr and Gabriel D A 1981 *Laser Light Scattering* (New York: Dover)
- Kernick D P, Tooke J E and Shore A C 1999 The biological zero signal in laser Doppler fluximetry—origins and practical implications *Pflugers Arch.* **437** 624–31
- Kienle A 2001 Non-invasive determination of muscle blood flow in the extremities from laser Doppler spectra *Phys. Med. Biol.* **46** 1231–44
- Leahy M J, deMul F F, Nilsson G E and Maniewski R 1999 Principles and practice of the laser-Doppler perfusion technique *Technol. Health Care* **7** 143–62A
- Liebert A, Leahy M and Maniewski R 1995 A calibration standard for laser-Doppler perfusion measurements *Rev. Sci. Instrum.* **66** 5169–73
- Liebert A, Lukasiewicz P, Boggett D and Maniewski R 1999 Optoelectronic standardization of laser Doppler perfusion monitors *Rev. Sci. Instrum.* **70** 1352–4
- Lohwasser R and Soelkner G 1999 Experimental and theoretical laser-Doppler frequency spectra of a tissuelike model of a human head with capillaries *Appl. Opt.* **38** 2128–37
- McCully K, Mancini D and Levine S 1999 Nuclear magnetic resonance spectroscopy: its role in providing valuable insight into diverse clinical problems *Chest* **116** 1434–41
- Nilsson G E 1984 Signal processor for laser Doppler tissue flowmeters *Med. Biol. Eng. Comput.* **22** 343–8
- Nilsson G E, Tenland T and Oberg P A 1980 Evaluation of a laser Doppler flowmeter for measurement of tissue blood flow *IEEE Trans. Biomed. Eng.* **27** 597
- Nossal R, Chen S-H and Lai C-C 1971 Use of laser scattering for quantitative determinations of bacteria motility *Opt. Commun.* **4** 35–9
- Obeid A N 1993 *In vitro* comparison of different signal processing algorithms used in laser Doppler flowmetry *Med. Biol. Eng. Comput.* **31** 43–52
- Smits G J, Roman R J and Lombard J H 1986 Evaluation of laser-Doppler flowmetry as a measure of tissue blood flow *J. Appl. Physiol.* **61** 666–72
- Soelkner G, Mitic G and Lohwasser R 1997 Monte Carlo simulations and laser Doppler flow measurements with high penetration depth in biological tissuelike head phantoms *Appl. Opt.* **36** 5647–54

- Sorensen C M, Mockler R C and O'Sullivan W J 1976 Depolarized correlation function of light double scattered from a system of Brownian particles *Phys. Rev. A* **14** 1520–32
- Steenbergen W and de Mul F F M 1998 New optical tissue phantom and its use for studying laser Doppler blood flowmetry *Proc. SPIE* **3196** 12–23
- Tenland T, Salerud E G, Nilsson G E and Oberg P A 1983 Spatial and temporal variations in human skin blood flow *Int. J. Microcirc. Clin. Exp.* **2** 81–90
- Ugurbil K, Hu X, Chen W, Zhu X H, Kim S G and Georgopoulos A 1999 Functional mapping in the human brain using high magnetic fields *Phil. Trans. R. Soc. B* **354** 1195–213